Seasonal predictability of daily rainfall characteristics in central-northern Chile for dry-land management

Koen Verbist
International Centre for Eremology, Dep. Soil Management, Ghent University, Ghent, Belgium
Water Centre for Arid Zones in Latin America and the Caribbean, La Serena, Chile

Andrew W. Robertson
International Research Institute for Climate and Society, Palisades, New York, USA

Wim M. Cornelis
International Centre for Eremology, Dep. Soil Management, Ghent University, Ghent, Belgium

Donald Gabriels
International Centre for Eremology, Dep. Soil Management, Ghent University, Ghent, Belgium

Note: The authors indicate the use of nonstandard references in the introduction of this manuscript that deal with the unpublished drought information of the region under study.

Corresponding author address: Koen Verbist, Dep. Soil Management, Coupure Links 653, 9000 Ghent Belgium.
E-mail: Koen.Verbist@UGent.be

Abstract

The seasonal predictability of daily rainfall characteristics relevant to dry-land management was investigated in the Coquimbo Region of central-northern Chile, with focus on May–August (MJJA) seasonal rainfall amount, daily rainfall frequency, and mean daily rainfall intensity at the station scale. The spatial coherence of interannual anomalies between stations was consistently found to be highest for the seasonal rainfall amount, indicative of potential seasonal predictability, with lower coherence for rainfall frequency and especially rainfall intensity. Three approaches to seasonal prediction with increasing complexity were tested. First, an index of the simultaneous El Niño-Southern Oscillation (ENSO) was regressed onto MJJA precipitation; this explained 32% of station-averaged rainfall-amount variability, but performed poorly in a forecasting setting. The second approach used retrospective seasonal forecasts made with three general circulation models (GCMs) to produce downscaled seasonal rainfall statistics by means of canonical correlation analysis (CCA). In the third approach, a Hidden Markov Model (HMM) was used to model stochastic daily rainfall sequences as a function of 4 daily rainfall "states," describing dry and progressively wetter conditions across the region, and to downscale daily station rainfall sequences from the GCM gridded seasonal averages. Similar cross-validated skill estimates were obtained using both downscaling methods, with the highest correlations with observations found for seasonal rainfall amount and rainfall frequency (up to 0.9 at individual stations). The downscaled hindcasts were then tailored to drought prediction, using the Standardized Precipitation Index (SPI) based on seasonal values, and the frequency of substantial rainfall days (>15mm; FREQ15) and the daily Accumulated Precipitation Deficit. Deterministic hindcasts of SPI showed high hit rates, with high Ranked Probability Skill Score for probabilistic hindcasts of FREQ15 obtained via the HMM.

1. Introduction

Climate variability can have serious societal impacts in semi-arid regions, especially for farmers who depend on rain-fed agriculture and on livestock production based on natural vegetation. In the Coquimbo Region in central-northern Chile, where rainfall amounts often drop under the limit for crop growth, a lack of rainfall results in a crisis situation for society. Over 2.6 million US Dollars was spent during 2007 to support affected families and farmers in the Coquimbo Region, to repair damage, to recover degraded soils and to increase irrigation programs (Chilean Ministry of Agriculture 2008, personal communication). Although these measures reduced the negative effects of the 2007 drought, they did not address all affected families due to budget limitations, nor did they increase preparedness and resilience to future droughts. Of the 16 307 rural families in Chile seeking monetary aid to overcome the negative aspects of the 2007 drought, more than 75% indicated suffering a lack of sufficient water for irrigation, for domestic use, and they observed harvest losses for the crops grown for their own consumption (Fondo de Solidaridad e Inversión Social (FOSIS) 2008, personal communication). A typical problem here is the lack of preparedness prior to these natural events, making any governmental action afterwards less cost effective. Despite the need, the current Drought Alleviation Plan formulated by the Chilean Government for the region (FOSIS 2008) does not include strategies for drought early warning, and the feasibility of such a system has yet to be demonstrated.

The El Niño Southern Oscillation (ENSO) is known to have a strong impact on winter rainfall over central-northern Chile, with positive rainfall anomalies during El Niño events, and below normal rainfall mostly associated with La Niña conditions (Aceituno 1988; Montecinos and Aceituno 2003; Pittock 1980; Quinn and Neal 1983; Rubin 1955; Rutllant

and Fuenzalida 1991). However, the associated seasonal predictability and forecast skill levels from current dynamical seasonal prediction models (e.g. Goddard et al. 2003) have not yet been assessed in detail for the statistics of local daily weather that are likely to be most pertinent to drought.

In this paper we document the characteristics of daily winter rainfall from station observations over the Coquimbo Region, and assess their seasonal predictability from three current seasonal prediction general circulation models (GCMs), together with statistical techniques to "downscale" and tailor the output from these relatively course resolution models to the station scale. Our analysis of the station rainfall data begins with a decomposition of seasonal rainfall amounts into rainfall frequency and the mean rainfall amount falling on wet days, i.e. the rainfall intensity. Rainfall frequency at local scale has been shown to be more spatially coherent in the tropics, and thus potentially more predictable on seasonal time scales (Moron et al. 2007), though it is not clear if this characteristic extends to midlatitudes. For a homogeneous region, the spatial coherence of seasonal anomalies across the region provides a measure of the potential seasonal predictability because there is no reason for the seasonal anomalies to differ between locations, except due to local scale unpredictable noise (Moron et al. 2007). Even in regions of complex terrain like Coquimbo, high spatial coherence would be an indicator of potential predictability. Rainfall frequency has also found to be more closely related to expected crop yields in some cases, due to the large runoffs associated with heavy rainfall events, especially in semi arid areas where storage by vegetation is small and soil infiltration rates low (Verbist et al. 2009).

To gain insight into the nature of the daily rainfall variability and its year-to-year modulations in more detail, we model the sequences of station rainfall in terms of different

daily rainfall types, using a hidden Markov model (HMM). The HMM provides an intuitive as well as quantitative probabilistic description of daily rainfall at a network of stations. In its non-homogeneous from (nHMM), in which exogenous variables are introduced to modulate the transition probabilities between states as a function of time, it can be used to downscale GCM seasonal predictions to obtain well-calibrated daily rainfall sequences at the station scale (Charles et al. 1999; Robertson et al. 2004, 2006, 2009). Encouraging results were reported by Bellone et al. (2000), who used a combined climate index, including wind, temperature and relative humidity fields, together with a nHMM to construct a model for daily rainfall amounts. In addition to probabilistic downscaling using the nHMM, we apply a simpler method based on canonical correlation analysis (CCA) to the seasonally-averaged statistics themselves (seasonal amount, daily rainfall frequency, and mean daily intensity), in order to obtain downscaled estimates of their seasonal predictability.

The work in this paper aims to lay the foundations for constructing drought early warning systems, through analyses of daily rainfall and by estimating seasonal predictability. The rainfall data and GCMs are described in Sect. 2, with the statistical methods outlined in Sect 3. The results of the station rainfall analyses and retrospective forecasts of drought indices are presented in Sect. 4, with the concluding remarks in Sect. 5.

2. Data

a. Observed rainfall data

The analysis of daily rainfall was based on data from 42 stations in the Coquimbo Region, obtained from the Chilean Water Authority (DGA) covering the period 1937–2006. However, it should be noted that data series were only available for a limited number of stations during

the first part (1937–1958) of this period (Fig.1).

Figures 2 and 3 show the average seasonality and spatial distribution of rainfall, together with a decomposition of seasonal rainfall amount into the frequency of occurrence of daily rainfall, and the mean daily intensity of rainfall on wet days (>1 mm). A distinct wet season covering the period May-August (MJJA) accounting for 85% of the annual rainfall amount was identified in the data set (Fig.2) and was used for further analysis. Rainfall intensities were on average higher during the wet season, reaching daily rainfall amounts of 207 mm in extreme cases. In terms of the seasonality within the MJJA season, average rainfall intensities are approximately constant, while rainfall frequency shows a clear seasonal modulation with a peak in July.

Spatial rainfall characteristics in the Coquimbo region for this period are given in Fig.3, indicating clear geographical modulation of rainfall. Seasonal rainfall amounts range between 43 mm in the north and 270 mm in the pre-Andean cordillera respectively (at 840 m above sea level), tending to increase eastward towards the Andes, due to orographic effects, and from north to south, due to an increased influence of the midlatitude storm track. Rainfall frequency is very low, ranging from 4 to 13 wet days per season on average, and is more geographically modulated than mean rainfall intensity (range of 10 – 24 mm per day). The larger spatial variation of rainfall frequency compared to mean intensity is consistent with the smaller within-season monthly modulation of the latter in Fig. 2, and with the frontal nature of winter rainfall over the region (Aceituno 1988).

b. Seasonal forecast models

Retrospective seasonal MJJA precipitation forecasts initialized on April 1 were obtained from

three GCMs: the European Centre Hamburg Model (ECHAM 4.5) (Roeckner et al. 1996), the National Centers for Environmental Prediction (NCEP) Climate Forecast System (CFS) (Saha et al. 2006) and the Community Climate Model (CCM 3.6) (Hurrell et al. 1998). The ECHAM and CCM are atmospheric GCMs that are both driven with the same constructed-analog (CA) predictions of sea surface temperature (SST) in a two-tiered approach (Li and Goddard 2005). We thus refer to them in the following as ECHAM-CA and CCM-CA respectively. The CFS is a coupled ocean-atmosphere GCM with initialization of the atmosphere, ocean and land-surface conditions through data assimilation. For all models, the ensemble mean (over 24 members for ECHAM and CCM and 15 members for CFS) gridded precipitation was used at a resolution ~1.9^{o} (CFS) and ~2.8^{o} (ECHAM-CA and CCM-CA) over the domain 20°–40°S and 65°–85° W for the 1981–2005 period.

3. Statistical methods

a. Spatial coherence analysis

Estimates of spatial coherence of interannual rainfall station anomalies are used as indicators of potential seasonal predictability following Moron et al. (2007). The number of spatial degrees of freedom (DOF) gives an empirical estimate of the spatial coherence in terms of empirical orthogonal functions (EOFs), with higher values denoting lower spatial coherence:

$$DOF = \frac{M^2}{\sum_{j=1}^{M} e_j^2} \qquad \text{(Eq. 1)}$$

where e_j are the eigenvalues of the correlation matrix formed from the M station seasonal-mean time series.

A second measure of the spatial coherence of interannual anomalies is given by the interannual variance of the Standardized precipitation Anomaly Index (var[SAI]), which is constructed from the station average of the standardized rainfall anomalies (Katz and Glantz 1986):

$$\mathrm{var}[SAI_i] = \mathrm{var}\left[\frac{1}{M}\sum_{j=1}^{M}\frac{\left(x_{ij} - \bar{x}_j\right)}{\sigma_j}\right] \qquad \text{(Eq. 2)}$$

where $\bar{x}_j$ is the long-term time mean over i=1,..,N years and σ_j is the interannual standard deviation for station j. The var[SAI] is a maximum when all stations are perfectly correlated (var[SAI]=1) and a minimum when the stations are uncorrelated, resulting in a var[SAI]=1/M.

b. Hidden Markov Model (HMM)

A state-based Markovian model was used to model daily rainfall sequences at the 42 stations, in order to gain insight into the daily rainfall process, and as a means to downscale daily rainfall sequences. We use the approach developed by Hughes and Guttorp (1994) for rainfall occurrence, while additionally modeling rainfall amounts. The hidden Markov model used here is described fully in Robertson et al. (2004, 2006). In brief, the time sequence of daily rainfall measurements on the network of stations is assumed to be generated by a first-order Markov chain of a few discrete hidden (i.e. unobserved) rainfall "states". For each state, the daily rainfall amount at each station is modelled here by a delta function at zero amount to model dry days, and an exponential to describe rainfall amounts on days with nonzero rainfall. To apply the HMM to downscaling, a nonhomogeneous HMM (nHMM) is used to generate an ensemble of daily rainfall sequences, in which the transition probabilities between states are modelled as functions of predictor variables, in our case GCM predictions of MJJA

seasonal-average precipitation over the region [5°S–40°S, 100°W–50°W]. A principal components analysis was first applied to the gridded data, selecting here the leading PC as the input variable to the nHMM. The nHMM was trained under leave-three-years-out cross-validation, using the CFS 15-member ensemble mean. To make downscaled simulations, we used each CFS ensemble member in turn, and generated 10 stochastic realizations for each one, yielding an ensemble prediction of 150 daily rainfall sequences for each MJJA season, providing a probabilistic forecast (Robertson et al. 2008).

The seasonal statistics of interest (seasonal amount, daily rainfall frequency, and mean daily intensity on wet days) were then computed from these simulated rainfall sequences and compared to their observed counterparts.

c. Downscaling of seasonal forecasts using canonical correlation analysis (CCA)

In addition to the nHMM, downscaling was also carried out by applying canonical correlation analysis (CCA) directly to the seasonal rainfall statistics of interest. The CCA regularizes the high-dimensional regression problem between a spatial field of predictors and predictands by reducing the spatial dimensionality via principal component (PC) analysis and thus minimizes problems of overfitting and multicolinearity (Tippett et al. 2003). Cross validation was used to determine the truncation points of the PC and CCA time series, via the Climate Predictability Tool (CPT) software toolbox (http://iri.columbia.edu/outreach/software/). As predictor data sets the retrospective seasonal MJJA precipitation forecasts by the three GCMs discussed in section 2b were used in conjunction with the MJJA seasonal rainfall at the 42 stations of the Coquimbo Region. The three CCA models were trained and tested over the 1981–2000 period, with a cross-correlation window of 5 years (i.e. leaving out two years on either side of

the verification value). As employed here, the CCA provides a deterministic *mean* forecast value, in contrast to the nHMM probabilistic ensemble.

4. Results

a. Spatial coherence of rainfall anomalies

As a first step towards assessing the seasonal predictability of rainfall at local scale, we begin with an analysis of spatial coherence, for each or the three rainfall characteristics: seasonal amount, rainfall frequency, and mean daily intensity. Based on Fig. 3, spatial coherence estimates were made separately for the three provinces (from north to south: Elqui, Limari and Choapa) and for three altitude classes (from west to east: 0–500 m, 500–1500 m and >1500m) (Fig. 3). Table 1 shows both the Degrees of Freedom (DOF) and the variance of the Standardized Anomaly Index (SAI) for these sub data sets. The highest DOF and lowest var[SAI] was observed for the Elqui Province in the north, indicating lowest spatial coherence of seasonal anomalies, consistent with its more arid nature and more sporadic rainfall. A similar tendency was found when looking at altitude influences, with lowest spatial coherence at highest altitudes (>1500m), due to orographic influences on rainfall variability.

The dependence of spatial coherence characteristics was analysed as a function of time scale using station autocorrelation. Fig. 4 shows the averaged Pearson correlation between each station pair plotted against distance, for rainfall amount, intensity and frequency averaged over several different time windows from daily to seasonal. Taking a value of 1/e (0.37) as the decorrelation distance (Dai et al. 1997; Moron et al. 2007; New et al. 2000; Ricciardulli and Sardeshmukh 2002; Smith et al. 2005), anomalies of rainfall amount were found to be significantly correlated at all temporal scales for all stations in the region. A similar

observation can be made for rainfall intensity. Rainfall frequency is uncorrelated beyond 150 km for the daily and 2-daily time scales, but becomes more highly correlated on longer time scales. The increase in spatial correlation on longer time scales observed for both rainfall amount and frequency, but not for intensity, was also found by Moron et al. (2007) for tropical rainfall. This increase toward the seasonal scale indicates a common regional seasonal climate forcing on these two rainfall characteristics. The spatial autocorrelation function is near-linear and time integration makes the stations more coherent, indicating that the seasonal function is a superposition of daily and seasonal effects, and also that the daily rainfall shows an organized, regional pattern repeated across the season.

While rainfall intensity appears just as coherent at the daily scale, it does not exhibit any increase in coherence when integrated over time. A distance of 200 km could be identified as the decorrelation distance for rainfall intensities between two stations in the Region. This is much larger than found by Moron et al. (2007) in the tropics, but is consistent with the advective character of rainfall in the Coquimbo Region, associated with extratropical cyclones with large spatial scales (Montecinos and Aceituno 2003). The examination of spatial coherence statistics in this sub-section indicates that seasonal rainfall amounts and frequencies are likely to be more predictable than mean daily rainfall intensities. However, the differences in spatial coherence between these three seasonal quantities is somewhat less than that found by Moron et al. (2007) in tropical regions.

b. Daily rainfall states

Given the high spatial coherence of rainfall in the Region, we next look in more detail at the evolution of daily rainfall by identifying a small set of typical daily rainfall states (or patterns) and the transitions between them from day to day, using a hidden Markov model. To

identify an appropriate number of rainfall states, the log-likelihood of HMMs was computed under cross-validation with up to 10 states, resulting in an increase in log-likelihood for a small number of states, levelling off at higher numbers. This is typical because the rainfall process in nature is more complex than the simple HMM, so that models with more parameters fit the observed rainfall data better, even under cross-validation. For diagnostic purposes, however, we seek a model with a small number of states for interpretability, and a model based on four rainfall states was thus chosen as a compromise. Using the maximum likelihood approach, the HMM parameters were estimated from the entire data set of 7872 days, measured at the 42 rainfall stations, applying the iterative expectation-maximization (EM) algorithm (Dempster et al. 1977; Ghahramani 2001). The algorithm was initialized 10 times from random seeds, selecting the run with the highest log-likelihood.

The four rainfall states thus obtained are shown in Fig. 5 in terms of their rainfall, showing the probability of rainfall occurrence at each station (panels a–d), and the average rainfall intensity on wet days (panels e–h). States were ordered from overall driest to wettest, showing a dry state 1 with rainfall probabilities near zero at all stations, and three states with increasing probabilities for rainfall and generally larger rainfall amounts on wet days. The spatial pattern of State 2 resembles that of the mean characteristics seen in Fig. 3, with more-frequent rainfall in the south and at higher altitudes. State 3 represents the rainfall events where rainfall is probable at most locations excluding the most northern ones, while rainfall intensities remain relatively small. State 4 can be interpreted as the ‘very wet’ state, with high rainfall probabilities over the whole region, and large rainfall intensities.

When looking at the matrix of day-to-day transition probabilities between the four states (Table 2), it can quickly be seen that state 1 is the most persistent state, but it is also the state

to which the wetter states 2 and 3 are most likely to evolve. State 4, the very wet state, has an almost equal probability for each of the states to follow it, indicating that states 2 and 3 tend to be intermediate in the transitions from a wet period to a dry period.

A visual interpretation of the temporal evolution is given in Fig. 6, showing the most probable daily sequence of the four states over the 64-summer period, obtained using the dynamical programming 'Viterbi' algorithm (Forney 1978). This resulted on average in 105 days of state 1 occurrence (85.4%), 10 days of state 2 (7.7%) and 5 days of state 3 (4.2%), whereas the 'very wet' state 4 occurred on only 3 days (2.7%) on average during each MJJA season of the 64 year period, but on average 56% of total seasonal rainfall was observed on these days. There is no obvious seasonality apparent in the Viterbi sequence, giving a rather random distribution of the states during the season.

The Viterbi state sequence also allows atmospheric circulation patterns to be associated with each state, enabling further physical interpretation. In Fig. 7 sea-level pressure fields from the NCEP-NCAR reanalysis data (Kalnay et al. 1996) were averaged over the days falling into each of the four rainfall states, showing average conditions for each state. Each composite is plotted as an anomaly from the long term MJJA average. The wet states 2–4 are all associated with a synoptic-scale wave, with an anomalous trough over the Chilean coast, extending east of the Andes. The pattern and phase of the wave are similar in each wet state, increasing in amplitude with the wetness of the state. Thus, the different rainfall types represented by the HMM states are primarily a function of the strength of the synoptic disturbance, rather than its phase. The tendency seen in the Viterbi sequence for multi-day persistent events made up of several states suggests this synoptic pattern, once established, often remains approximately stationary while growing and decaying in situ.

c. ENSO influence on seasonal rainfall characteristics

The interannual variability over the Coquimbo Region can be interpreted in terms of the HMM's state sequence, with more instances of the wetter states during wet winters. Before proceeding with that analysis, we first summarize the well-known ENSO influence on the seasonal statistics of rainfall (MJJA amount, rainfall frequency, and mean daily intensity) averaged over all 42 stations. The relationship between seasonal rainfall amounts and ENSO is plotted in Fig. 8 in terms of the Niño 3.4 index. There is a clear tendency for above normal rainfall to be associated with the warm ENSO phase and vice versa. Nevertheless, several years have less than normal rainfall without strong La Niña characteristics. The Pearson correlation between Niño 3.4 and MJJA rainfall amount for the entire period 1937–2006 is 0.57, which is statistically significant at the 99% level according to a two-sided Student test. When only ENSO years are included, as defined by those years where 50% of the MJJA months were marked as ENSO using the Bivariate ENSO or BEST Index (Smith and Sardeshmukh 2000), the correlation increases to 0.80, which is indicative for the strength of the ENSO signal in extreme wet or dry years.

Table 3 shows the correlations between the observed station-averaged MJJA rainfall amount, frequency and intensity and the cross-validated hindcasts from multiple linear regressions with the Niño 3.4 index averaged over different time periods as a predictor. Correlations are strongest when the Niño 3.4 index is contemporaneous or follows the MJJA season, consistent with the so-called ENSO spring predictability barrier around May; once established during boreal summer, ENSO events tend to persist into the following boreal fall. The hindcasts with the FMAM averaged Niño 3.4 index or even for individual months March, April and May, were only weakly correlated with the MJJA total rainfall data, with Pearson correlations of

0.26, 0.15, 0.32 and 0.44 respectively, limiting the prediction potential of the Niño 3.4 index. Similar behaviour was found for rainfall frequency, with highest Pearson correlation for the contemporaneous period, whereas rainfall intensity was weakly correlated when using the ENSO index as a predictor for all periods considered (Table 3).

d. ENSO influence on rainfall states

Year-to-year variations in the frequency of HMM state occurrence are plotted in Fig.9. The correlations between state-frequency and the MJJA Niño 3.4 index are -0.44, 0.27, 0.18 and 0.52 respectively (all are significant at the 95% level, except for state 3). Thus the ENSO relationship discussed above is mostly expressed in terms of the frequency of occurrences of states 1 and 4. This is remarkable, given the small number of days falling into state 4, and its association with the most-intense storms.

El Niño events tend to weaken the subtropical anticyclone and to displace the frontal storms to more northern locations than normal with a blocking of their usual path further to the south (Garreaud and Battisti 1999; Rutllant and Fuenzalida 1991). This is consistent with our finding of a positive correlation between the occurrence of the three wet states and the ENSO index. When evaluating wet years, Rutllant and Fuenzalida (1991) found that a low-pressure zone becomes established over Central Chile and Northwestern Argentina, separating the Pacific anticyclone from the Atlantic high pressure area, which is consistent with the observed atmospheric circulation patterns observed for states 2 to 4 that exhibit an anomalous synoptic trough between 30°–40°S, and a ridge to the south (Fig.7).

e. Seasonal prediction of daily rainfall aggregates

Given the impact of ENSO on Coquimbo-region rainfall documented in the previous sub-sections, we next explore seasonal predictability of the latter based on GCM retrospective forecasts. In this subsection we consider the seasonal aggregate scale, using the canonical correlation analysis (CCA) described in Sect 3c, to regress the GCM seasonal-average rainfall predictions onto the observed station seasonal rainfall statistics presented in Sect 4c. Scatterplots of the cross-validated seasonal rainfall deterministic forecasts are shown in Fig. 10 over the hindcast period (1981–2000) for each of the three GCMs, where each circle represents the forecast mean of the seasonal rainfall amount for each station-year. A clear deviation from the 1:1 line is observed for the ECHAM-CA model, indicating clear underestimation of the higher rainfall amounts observed during wet years. The CCM-CA model shows an overestimation at the lower rainfall amounts, while failing to predict the more extreme rainfall values. The CFS model performs best, showing the least scatter as well as quite successful predictions in the higher range of rainfall amounts. This is confirmed by Table 4, which gives the station-averaged root mean square error (RMSE), mean error or bias (ME), and Pearson anomaly correlation coefficients for each of the model (cross-validated) retrospective forecasts of station precipitation. The CCM-CA gave the lowest correlation and the highest RMSE, but was the least biased, with a low ME. Correlation was higher for the ECHAM-CA, but ME and RMSE indicated an important bias in comparison to the other models. The CFS model showed the highest correlation coefficient and a low RMSE, but with a negative ME, underestimating the observed rainfall amounts at the highest observed rainfall amounts (e.g. 36% at 500mm). Nevertheless, the CFS model was selected for further processing, due to its superior correlation statistics.

The Pearson correlation skill map from CFS for all stations (Fig. 11) shows a good correlation between observed and hindcast precipitation for almost all stations, with individual correlations between 0.57 and 0.80. A similar picture emerges for rainfall frequency, with slightly lower Pearson skill (0.20–0.63), while the correlation coefficients for rainfall intensity are generally much lower (from -0.15 until 0.64).

f. Seasonal prediction of stochastic daily rainfall sequences

Having addressed the seasonal predictability of daily rainfall aggregates (seasonal amount, rainfall frequency, and mean daily intensity) in the previous subsection, we next use a nHMM to derive seasonal forecasts of stochastic daily rainfall sequences at each of the stations. The nHMM used here builds on the HMM results presented in Sect 4b, but with the inclusion of CFS forecasts of MJJA seasonal-average precipitation, as described in Sect. 3b. This is the same CFS predictor field used via CCA in the previous subsection.

The resulting daily rainfall simulations were then used to construct the seasonal rainfall amount, rainfall frequency, and mean daily intensity, and the ensemble averages then correlated with observed values (Fig.12). As in the case of the CCA-based forecasts in Fig. 11, correlations were generally higher for seasonal rainfall amount and rainfall frequency, compared with rainfall intensity, with station values ranging from 0.17–0.92, 0.19–0.92 and -0.38–0.84 for the three quantities respectively. Inter-station differences in skill are larger than in the CCA approach, but fewer stations with negative correlations were obtained using the nHMM (note that only positive values are plotted in Figs. 11 and 12).

Time series of the station-averaged MJJA seasonal rainfall statistics are plotted in Fig. 13, which compares the median and interquartile range of the 150-member ensemble of nHMM

simulations, together with the observed values and CCA-based hindcasts. The hindcasts of seasonal rainfall amount obtained using both methods (CCA and nHMM) follow the observed highs and lows reasonably well (Fig. 13a), with a Pearson correlation skill for the nHMM mean of 0.62. A small overestimation for the nHMM low rainfall amount years is observed, as well as an underestimation when dealing with very wet years, and can be attributed to the deviations observed between the CFS model predicted and observed precipitation (Table 4 and Fig. 10).

Rainfall frequency hindcasts from the nHMM also proved to be skillful (ρ=0.55), representing the observed interannual variability better than for rainfall intensity (ρ=0.30). Rainfall intensity did not closely follow the ENSO index, although higher intensities were observed during ENSO years. The underestimated mean rainfall intensities in 1984, resulted in an important underestimation of the seasonal rainfall amount, while the CCA hindcast of seasonal amount was less affected. The year 1983, on the other hand, showed more rainfall days but with low intensities, than picked up by the nHMM, still resulting in an acceptable prediction of the seasonal rainfall amount.

g. Towards a Drought Early Warning System

Although no effort was made to design or setup a drought early warning system for the Coquimbo Region, this paper tries to identify the prediction potential that would be essential to such an effort. In order to tailor our rainfall hindcasts more specifically to drought indicators, we firstly express our hindcasts in terms of the Standardized Precipitation Index or SPI (Edwards and McKee 1997; McKee et al. 1993), a commonly used drought classification method. The SPI is derived by transforming the probability distribution of (here seasonal amount) rainfall into a unit normal distribution so that the mean SPI is zero and each value

is categorized in one of its 5 quantiles and as such given a 'drought class'. The SPI hindcasts derived from the CFS using the CCA and nHMM methods are shown in Fig. 14, together with those derived from the (simultaneous) regression with MJJA Niño 3.4 SST. Each of the methods was able to represent observed SPI variability rather well, although different SPI classes were often predicted. This is reflected in Table 5, where fits between observed and simulated SPIs are expressed in terms of ρ, ME, RMSE and hit rate. None of the prediction models showed a significant bias, due to the standardization of the SPI, and the Pearson correlation values are similar to those of the seasonal rainfall amount. The hit rate measures the success of the method to predict the SPI class, and substantially exceeds the 20% rate expected by chance. The hit rate increased to values of 92%, 92% and 88% for the ENSO Index, the CFS method and the nHMM respectively, when an error of one SPI class is accepted, indicating that the general trend (dry, wet or normal) is maintained by the three methods.

In a second approach, the nHMM hindcasts of daily rainfall series were converted into four daily drought indices and compared with observed values. As a first index, the frequency of days with substantial rainfall (>15 mm per day) was used to classify years with drought risk, hereafter named FREQ15. A second set of drought indices based on daily rainfall were derived from the work of Byun and Wilhite (1999), using the Effective Precipitation (EP) concept to represent the soil water storage at each day during the wet season. After evaluating all proposed indices, three were retained, based on their higher sensitivity to observed drought in the region. The first is the Accumulated Precipitation Deficit (APD), which gives a simple accumulation of daily precipitation deficit from May to August, and was found to be a good measure for drought intensity. The second is the Accumulation of Consecutive days of Negative Standardized EP, further named ANES, and is a measure for accumulated stress

during droughts (Byun and Wilhite 1999). The last is the Effective Drought Index or EDI, which gives a drought classification similar to the SPI, with positive values indicating surplus rainfall and negative values dry or drought conditions.

In general, the drought indices obtained from the nHMM cross-validated hindcasts closely followed the observed indices for the period 1981–2005. The fit proved best for the FREQ15 and the APD index (ρ=0.63 and 0.60 resp.), compared with the EDI and ANES (ρ= 0.51 and 0.50). The observed versus predicted values of FREQ15 and APD are plotted in Fig. 15, which shows the median and the inter-quartile range (IQR) of the nHMM ensemble, showing information about the predicted distributions. The spread of the forecasts can be evaluated in terms of the IQR, which should bracket the observations in 50% of the years to be well calibrated, with lower values indicating too little spread and with values above 50% for those forecast distributions with too much spread. The IQR were determined, resulting in a value of 44% and 52% of the years respectively, indicating that the forecasts are rather well calibrated.

To quantify the skill of these probabilistic forecasts, the Ranked Probability Skill Score (RPSS) is used, which is a squared error metric that allows measuring the distance between the cumulative distribution function of the forecast and the verifying observation, and is expressed with respect to a baseline given by the climatic forecast distribution. A perfect forecast would be represented by a RPSS of 100%, while negative values indicate that the forecast is less skillful than the climatological equal-odds forecast. For the four indices under consideration, the station average median RPSS values were 25.2 for FREQ15, 12.3 for APD, 12.7 for EDI and -2.6 for ANES, indicating better than climatology forecasts in the former three cases. Additionally, the percentage of positive RPSS values were found to be 84%, 80%, 64% and 48% respectively, confirming the better predictability of FREQ15 and APD, and

lower predictability for EDI and ANES. In Fig 16 the median RPSS is presented for each station for FREQ15 and APD, showing similar results as the station average, with few areal differences, but suggests a superior predictability of FREQ15 compared to APD.

Since FREQ15 and APD are well correlated to declared drought years in the Coquimbo region (Novoa-Quezada 2001), with both showing a correlation of 0.87, their relatively good predictability is especially encouraging for climate risk management purposes.

5. Summary and conclusions

Rainfall variability is known to be a mayor economic and social disruptor in the central-northern area of Chile, with large financial consequences for society when both extreme drought and extreme wet conditions occur. A low preparedness could be partly responsible for the large impact of these events. Therefore, a need was formulated to develop a climate risk management system for the semi-arid regions of Chile, to reduce the vulnerability and increase resistance to extreme climatic events. An early warning system for droughts and floods would be an essential component of such an approach, which requires estimation and prediction of the rainfall characteristics relevant to drought.

Winter rainfall characteristics in the Coquimbo Region of Chile were first investigated using daily rainfall records at 42 stations, with special attention to spatial and temporal characteristics and relationship with ENSO. Seasonal rainfall amounts, daily rainfall frequencies, and mean daily rainfall intensities all generally increase southward and eastward toward the Andes (Fig. 3). An analysis of the spatial correlations between stations (Fig. 4) indicated large inter-station correlations at the daily timescale, particularly for rainfall amount. The spatial coherence of rainfall amount and frequency was found to increase

substantially with temporal averaging, suggesting the role of ENSO forcing at the seasonal scale. Seasonal anomalies of mean daily rainfall intensity were found to be somewhat less spatially coherent (Table 1), though their coherence was larger than found by Moron et al. (2007) for tropical rainfall, due to the frontal character of rainfall in the region.

The spatio-temporal evolution of daily rainfall patterns across the region was further elucidated in terms of four rainfall "states" identified using a Hidden Markov Model (HMM); these states consisted of dry and increasingly wet conditions (Fig. 5), the latter associated with near-stationary trough in sea-level pressure, centered to the south and east of the region (Fig. 7). The daily sequences of these states showed sporadic rainfall events with little seasonality within the winter season (Fig. 6), while the likelihood of an intense storm across the region (state 4) was found to be strongly correlated with ENSO (Fig. 9), thus providing an interpretation in terms of daily weather for the well-established seasonal rainfall relationship with ENSO (Fig. 8).

Seasonal predictability of rainfall characteristics was explored firstly using a simple univariate index of ENSO, Niño 3.4 SST; this proved only to be well correlated for simultaneous (May or MJJA) values of the index, and thus not useful for prediction. Rainfall intensities were found not to be well correlated. Predictability was further explored using GCM retrospective forecasts of MJJA rainfall amounts initialized on April 1 of each year 1981–2005. Of three the GCMs considered (ECHAM-CA, CCM-CA and CFS), the highest skill and lowest bias was obtained for the CFS model, using CCA to downscale the forecasts to the station scale (Fig. 10; Table 4). The CFS was then downscaled using both CCA and the nHMM, and the skill examined at the station scale for seasonal rainfall amount, frequency, and mean daily intensity (Figs. 11–13). Similar results were obtained using both methods, with highest

correlations with observations were found for seasonal rainfall amount and rainfall frequency for most measuring stations in the region, with low or negative correlations for rainfall intensity.

The retrospective forecasts of rainfall were then tailored for drought prediction, using firstly the Standardized Precipitation Index (SPI) based on seasonal rainfall amount, and secondly for drought indices based on daily rainfall statistics, making use of the nHMM for the latter. The SPI was quite well forecast by both CFS-CCA and CFS-nHMM methods (Fig. 14). Four different daily drought indices were then constructed from the nHMM simulations, of which the frequency of occurrence of days exceeding 15 mm/day (FREQ15) and the accumulated daily precipitation deficit (APD) gave highest correlations with observations and positive prediction skill for all stations.

Downscaled seasonal predictions of seasonal rainfall characteristics and related drought indices have been shown feasible for the Coquimbo Region. This could be regarded as an important step in the development of a tailored climate risk management system that should contribute to reduce climate uncertainty in a region that is affected by high rainfall variability.

Acknowledgements

The authors would like to thank the Chilean Water Authority (Dirección General de Aguas) for providing the daily rainfall series of the Region. This research was funded by the Flemish Government, Department of Sciences and Innovation/Foreign Policy, the UNESCO Regional Office for Science and Technology in Latin America and the Caribbean, and by the US National Oceanic and Atmospheric Administration through a block grant to the IRI.

References

Aceituno, P., 1988: On the functioning of the Southern Oscillation in the South American sector. Part I: Surface climate. *Mon. Wea.Rev.*, 505-524.

Bellone, E., J. P. Hughes, and P. Guttorp, 2000: A hidden Markov model for downscaling synoptic atmospheric patterns to precipitation amounts. *Climate Res.*, **15,** 1-12.

Byun, H.-R., and D. A. Wilhite, 1999: Objective Quantification of Drought Severity and Duration. *J. Climate*, **12,** 2747-2756.

Charles, S. P., B. C. Bates, P. H. Whetton, and J. P. Hughes, 1999: Validation of downscaling models for changed climate conditions: case study of southwestern Australia. *Clim. Res.*, **12,** 1-14.

Dai, A., I. Y. Fung, and A. D. del Genio, 1997: Surface global observed land precipitations variations: 1900-1988. *J. Climate*, **10,** 2943-2962.

Dempster, A. P., N. M. Laird, and D. R. Rubin, 1977: Maximum likelihood from incomplete data via the EM algorithm. *J. R. Stat. Soc. B.*, **39,** 1-38.

Edwards, D. C., and T. B. McKee, 1997: Characteristics of 20th century drought in the United States at multiple time scales, Climatology Rep. 97–2, Department of Atmospheric Science, Colorado State University, Fort Collins, Colorado,155 pp.

Forney, G. D., 1978: The Viterbi algorithm. *Proc. IEEE*, **61,** 268-278.

FOSIS, 2008: Superando la sequía. Plan Especial para familias vulnerables de zonas rurales afectadas por la sequía, 11 pp.

Garreaud, R. D., and D. S. Battisti, 1999: Interannual (ENSO) and interdecadal (ENSO-like) variability in the Southern Hemisphere tropospheric circulation. *J. Climate*, **12,** 2113-2122.

Ghahramani, Z., 2001: An introduction to hidden Markov models and Bayesian networks. *Int. J. Pattern Recogn. Artif. Intell*, **15,** 9-42.

Goddard, L., A. G. Barnston, and S. J. Mason, 2003: Evaluation of the IRI's "Net Assessment" seasonal climate forecasts: 1997-2001. *Bull. Amer. Meteor. Soc.*, **84,** 1761-1781.

Hughes, J. P., and P. Guttorp, 1994: A class of stochastic models for relating synoptic atmospheric patterns to regional hydrologic phenomena. *Water Resour. Res.*, **30,** 1535-1546.

Hurrell, J. W., J. J. Hack, B. A. Boville, D. L. Williamson, and J. T. Kiehl, 1998: The dynamical simulation of the NCAR Community Climate Model version 3 (CCM3). *J. Climate*, **11,** 1207-1236.

Kalnay, E., and Coauthors, 1996: The NCEP/NCAR 40-Year Reanalysis Project. *Bull. Amer. Meteor. Soc.*, **77,** 437-471.

Katz, R. W., and M. H. Glantz, 1986: Anatomy of a rainfall index. *Mon. Wea. Rev.*, **114,** 764-771.

Li, S., and L. Goddard, 2005: Retrospective Forecasts with the ECHAM4.5 AGCM. IRI Technical Report 05-02. IRI, Palisades, NY.

McKee, T. B., N. J. Doesken, and J. Kliest, 1993: The relationship of drought frequency and duration to time scales. *Proceedings of the 8th Conference on Applied Climatology*, A. M. Society, Ed., 179-184.

Montecinos, A., and P. Aceituno, 2003: Seasonality of the ENSO-Related Rainfall Variability in Central Chile and Associated Circulation Anomalies. *J. Climate*, **16,** 281-296.

Moron, V., A. W. Robertson, M. N. Ward, and P. Camberlin, 2007: Spatial coherence of tropical rainfall at the regional scale. *J. Climate*, **20,** 5244-5263.

New, M., M. Hulme, and P. Jones, 2000: Representing twentiethcentury space-time climate variability. Part II: Development of 1901-96 monthly grids of terrestrial surface climate. *J. Climate*, **13,** 2217-2238.

Novoa-Quezada, P., 2001: Determinación de condición de sequía por análisis de la variación de humedad del horizonte radicular usando el modelo de simulación Hidrosuelo. CONAF, Viña del Mar, Chile, 44 pp.

Pittock, A. B., 1980: Patterns of climatic variation in Argentina and Chile. Part I: Precipitation, 1931-1960. *Mon. Wea. Rev.*, **108,** 1347-1361.

Quinn, W., and V. Neal, 1983: Long-term variations in the Southern Oscillation, El Niño and the Chilean subtropical rainfall. *Fish.Bull.*, **81,** 363-374.

Ricciardulli, L., and P. D. Sardeshmukh, 2002: Local time- and space scales of organized tropical deep convection. *J. Climate*, **15,** 2775-2790.

Robertson, A. W., S. Kirshner, and P. J. Smyth, 2004: Downscaling of daily rainfall occurrence over northeast Brazil using a hidden Markov model. *J. Climate*, **17,** 4407-4424.

Robertson, A. W., A. V. M. Ines, and J. W. Hansen, 2007: Downscaling of Seasonal Precipitation for Crop Simulation. *J. App Meteorol Clim*, **46,** 677-693.

Robertson, A. W., V. Moron, and Y. Swarinoto, 2009: Seasonal predictability of daily rainfall statistics over Indramayu district, Indonesia. *Int. J. Climatol.*, **29,** 1449-1462.

Robertson, A. W., S. Kirshner, P. C. Smyth, S. P. Charles, and B. C. Bates, 2006: Subseasonal-to-interdecadal variability of the Australian monsoon over North Queensland. *Q. J. R. Meteorol. Soc.*, **132,** 519-542.

Roeckner, E., and Coauthors, 1996: The atmospheric general circulation model ECHAM-4: Model description and simulation of present-day climate, 90 pp.

Rubin, M. J., 1955: An analysis of pressure anomalies in the Southern Hemisphere. *Notos*, **4,** 11-16.

Rutllant, J., and H. Fuenzalida, 1991: Synoptic aspects of the central Chile rainfall variability associated with the Southern Oscillation. *Int. J. Climatol.*, **11,** 63-76.

Rutllant, J., 2004: Large-scale atmospheric circulation features associated with the 1997-1999 ENSO cycle and their consequences in the central-Chile precipitation regime. *El Niño-La Niña 1997-2000. Its effects in Chile*, S. Avaria, J. Carrasco, J. Rutllant, and E. Yáñez., Eds., CONA, 61-76.

Saha, S., and Coauthors, 2006: The NCEP Climate Forecast System. *Journal of Climate*, **19,** 3483-3517.

Smith, C. A., and P. Sardeshmukh, 2000: The Effect of ENSO on the Intraseasonal Variance of Surface Temperature in Winter. *Int. J. Climatol.*, **20**, 1543-1557.

Smith, D. F., A. J. Gasiewski, D. L. Jackson, and G. A. Wick, 2005: Spatial scales of tropical

precipitation inferred from TRMM Microwave imager data. *IEEE Trans. Geophys. Remote Sens.*, **43,** 1542-1551.

Tippett, M. K., M. Barlow, and B. Lyon, 2003: Statistical correction of central Southwest Asia winter precipitation simulations. *Int. J. Climatol.*, **23,** 1421-1433.

Verbist, K., J. M. Baetens, W. M. Cornelis, D. Gabriels, C. Torres, and G. Soto, 2009: Hydraulic conductivity as influenced by stoniness in degraded drylands of Chile. *Soil Sci. Soc. Am. J.*, **73,** 471-484.

List of Figures

FIG. 1. Number of stations with May–August station rainfall data used in the analysis.

FIG. 2. Average rainfall seasonality in the Coquimbo Region; a) average number of wet days (>1mm) and b) average rainfall intensity (mm day^{-1}) on wet days with indication of the standard deviation (whisker).

FIG. 3. Average rainfall characteristics during the wet season (May–August): a) seasonal rainfall amount; b) rainfall frequency; and c) mean daily rainfall intensity for the period 1937–2006.

FIG. 4. Spatial correlation function of daily rainfall amount, rainfall intensity and rainfall frequency for the daily, 2-day, 5-day, 10-day, 30 day and seasonal averaging periods. The 1/e decorrelation value is shown as a dashed line.

FIG. 5. Four-state HMM rainfall parameters. (a)–(d): probabilities of rainfall occurrence and (e)–(h): mean rainfall intensities (i.e. wet-day amounts).

FIG. 6. The most probable HMM state sequence obtained using the Viterbi algorithm.

FIG. 7. Composites of sea-level pressure anomalies for each rainfall state (mb).

FIG. 8. Station-average MJJA rainfall amount, colored according to the sign and magnitude of the Niño 3.4 SST index for the period 1937–2005. .

FIG. 9. Frequency of occurrence of each rainfall state over the 1943–2006 period (black line). The ENSO Niño 3.4 index is also plotted in each panel (grey line), together with the Pearson

correlation coefficients (ρ). Standardized units.

FIG. 10. Cross-validated hindcasts versus observed precipitation amounts using CCA for the three GCMs for the period 1981–2000, where each circle represents the value for each station, for each year. Thus there are 42x20 circles in each panel.

FIG. 11. Pearson correlation between CFS hindcasts downscaled using CCA and observed rainfall for (a) seasonal rainfall amount, (b) rainfall frequency, and (c) mean rainfall intensity, for the period 1981–2005.

FIG. 12. As Fig. 11, but for CFS downscaled rainfall obtained using the nHMM and taking the ensemble mean over the 150 nHMM simulations.

FIG. 13. Comparison of station-averaged downscaling results obtained from CFS using CCA and the nHMM. (a) seasonal rainfall amount, (b) rainfall frequency (b), mean rainfall intensity. The error bars indicate the 25th and 75th percentiles of the simulated nHMM ensemble values. The Niño 3.4 index is also indicated.

FIG. 14. Station-averaged hindcasts of the Standardized Precipitation Index (SPI) obtained from the MJJA Niño 3.4 Index, and the CFS downscaled with CCA and with the nHMM. The SPI values constructed from observed station rainfall are also plotted.

FIG. 15. Hindcasts of two station-averaged drought indices (circles) consisting of (a) the number of days with rainfall exceeding 15mm (FREQ15), and (b) and the Accumulated (daily) Precipitation Deficit (APD), based on the nHMM simulations, compared with values constructed from observed daily rainfall (dashed). The error bars indicate the 25th and 75th percentiles of the nHMM ensemble. The Niño 3.4 index is also indicated.

FIG. 16. Median Rank Probability Skill Score (RPSS) for hindcasts of (a) the number of days with rainfall exceeding 15mm (FREQ15) and the Accumulated Precipitation Deficit (APD), constructed from the nHMM simulations.

Table 1 Degrees of freedom (DOF) and variance of the Standardized Anomaly Index (Var[SAI]) for seasonal rainfall amount (RAm), rainfall intensity (RI) and rainfall frequency (RF) for each province and altitude class in the Coquimbo Region

		DOF			Var[SAI]		
	N†	RAm	RI	RF	RAm	RI	RF
Province							
Elqui	12	9.14	17.26	11.85	0.30	0.20	0.26
Limari	24	4.07	7.13	5.10	0.44	0.31	0.40
Choapa	8	5.14	7.17	6.18	0.41	0.34	0.37
Altitude class							
0–500 m	13	5.05	8.91	6.33	0.40	0.28	0.36
500–1500 m	25	5.10	7.86	6.38	0.40	0.31	0.35
>1500 m	6	13.57	21.01	15.09	0.23	0.16‡	0.21

† Number of stations used

‡ Minimum Var[SAI] value (mean correlation equals zero)

Table 2 Transition matrix for the 4-state HMM. "From" states occupy the rows, "To" states the columns. Thus, the probability of a transition from state 2 to state 1 is 0.56.

	To State			
From State	1	2	3	4
1	0.92	0.05	0.02	0.01
2	0.56	0.22	0.12	0.09
3	0.47	0.25	0.19	0.09
4	0.23	0.28	0.22	0.27

Table 3 Pearson correlation coefficients between the observed station-averaged seasonal rainfall amounts (RAm), rainfall frequencies (RF) and rainfall intensities (RI), and the cross-validated hindcasts using the average Niño 3.4 index (1937-2006) for different months and multi month periods as a predictor.

	Average Niño 3.4 Index					
	FMAM	March	April	May	MJJA	NDJF
RAm	0.26	0.15	0.32	0.44	0.57	0.39
RF	0.33	0.23	0.36	0.49	0.59	0.39
RI	-0.29	-0.42	-0.09	0.03	0.20	0.19

Table 4 Pearson correlation coefficient (ρ), mean error (ME) and root mean squared error (RMSE) for cross-validated CCA hindcasts of seasonal rainfall amount with the ECHAM-CA, CFS and CCM-CA models for the period 1981-2000.

	ρ (-)	ME (mm)	RMSE (mm)
ECHAM-CA	0.41*	-9.74	133.54
CFS	0.69*	-8.45	99.92
CCM-CA	0.17*	-2.24	137.73

* Correlation is significant at α=0.05

Table 5 Pearson correlation coefficient (ρ), mean error (ME), root mean squared error (RMSE) and hit rate for hindcasts expressed in terms of the station-averaged Standardized Precipitation Index. The hindcasts were made based on the MJJA Niño 3.4 Index, and the CFS downscaled with CCA or the nHMM.

	Niño 3.4 Index	CCA	nHMM
ρ	0.56	0.65	0.58
ME	-0.01	-0.01	0.00
RMSE	0.17	0.17	0.18
Hit Rate† (%)	68.0	56.0	60.0

† Defined as the percentage of correct SPI class prediction

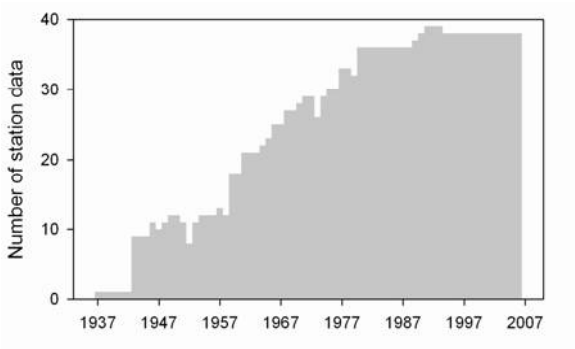

FIG. 1. Number of stations with May–August station rainfall data used in the analysis.

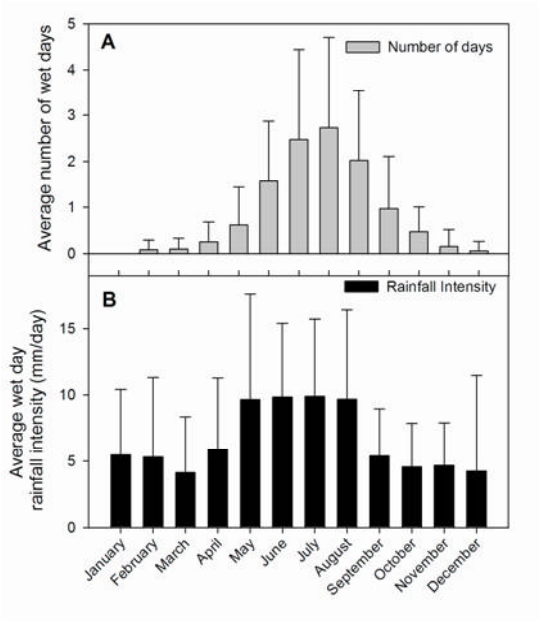

FIG. 2. Average rainfall seasonality in the Coquimbo Region; a) average number of wet days (>1mm) and b) average rainfall intensity (mm day^{-1}) on wet days with indication of the standard deviation (whisker).

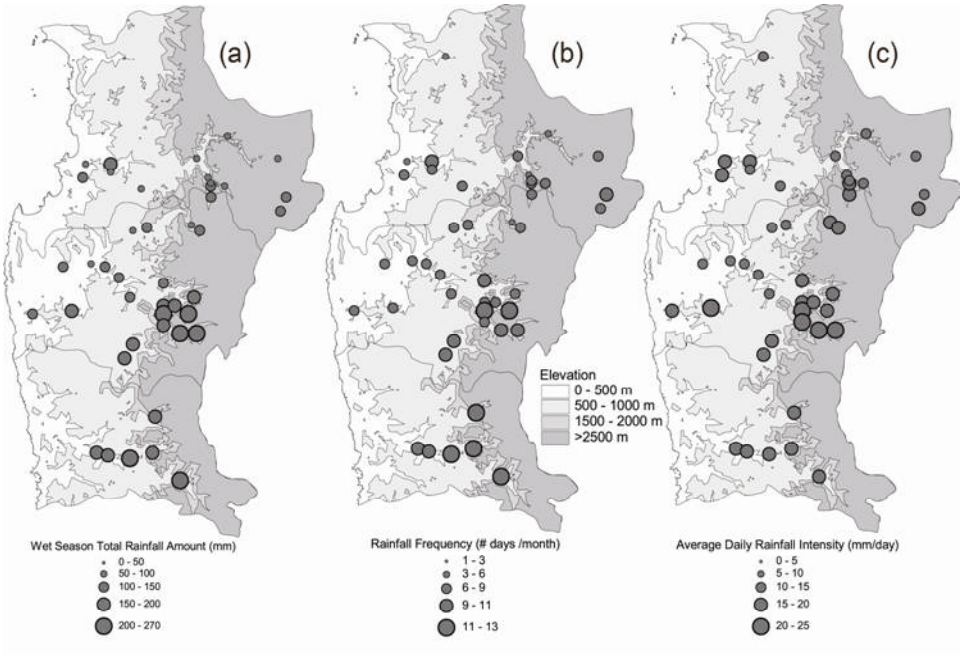

FIG. 3. Average rainfall characteristics during the wet season (May–August): a) seasonal rainfall amount; b) rainfall frequency; and c) mean daily rainfall intensity for the period 1937–2006.

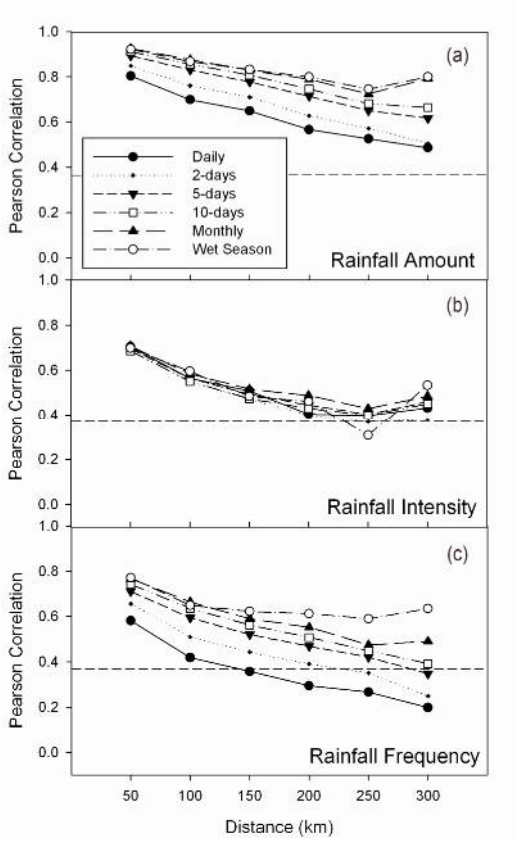

FIG. 4. Spatial correlation function of a) daily rainfall amount, b) rainfall intensity and c) rainfall frequency for the daily, 2-day, 5-day, 10-day, 30 day and seasonal averaging periods. The 1/e decorrelation value is shown as a dashed line.

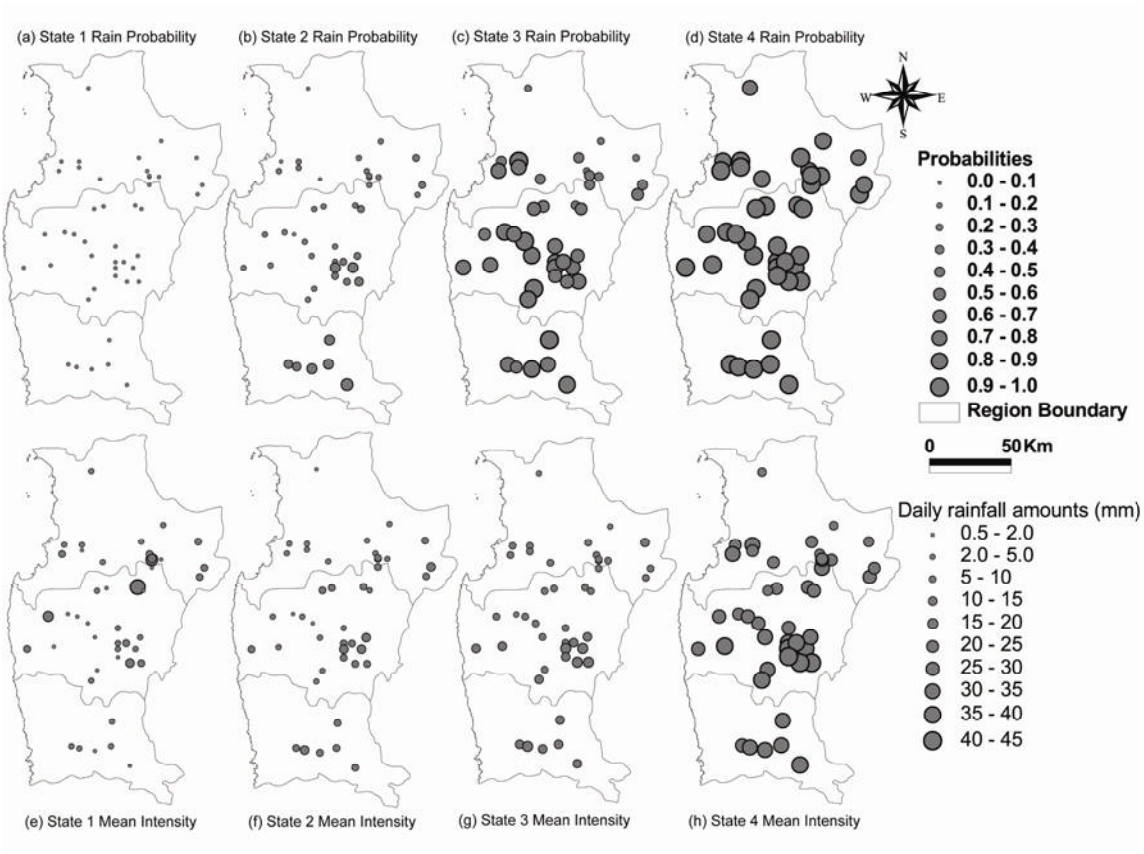

FIG. 5. Four-state HMM rainfall parameters. (a)–(d): probabilities of rainfall occurrence and (e)–(h): mean rainfall intensities (i.e. wet-day amounts).

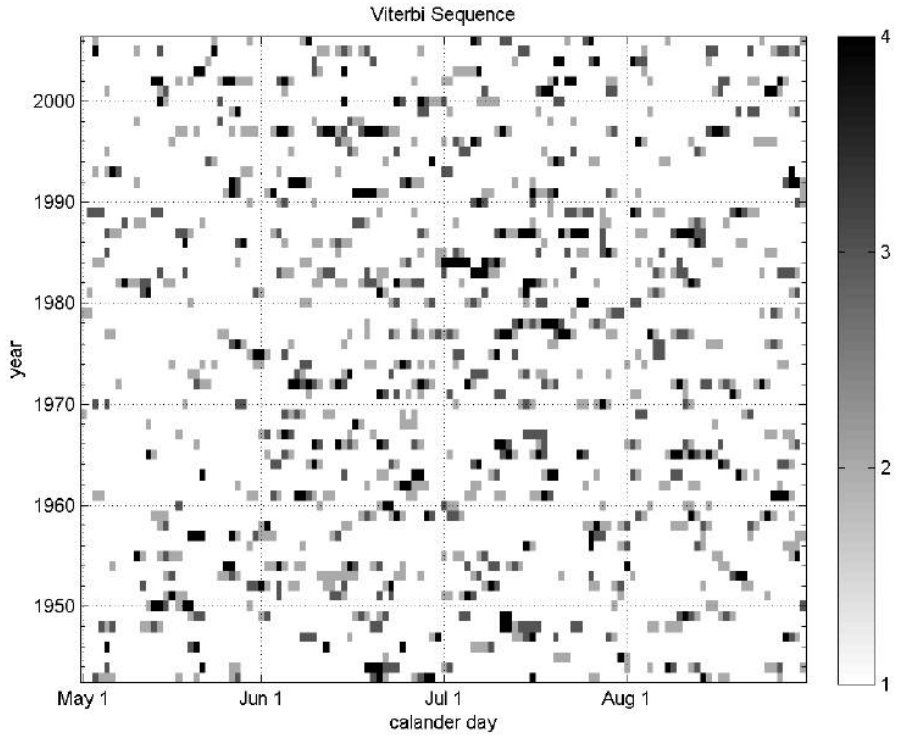

FIG. 6. The most probable HMM state sequence obtained using the Viterbi algorithm.

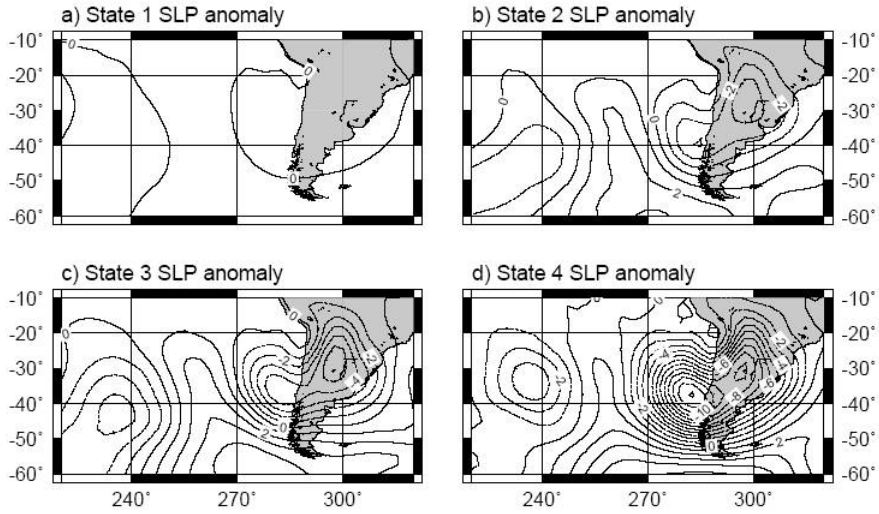

FIG. 7. Composites of sea-level pressure anomalies for each rainfall state (mb).

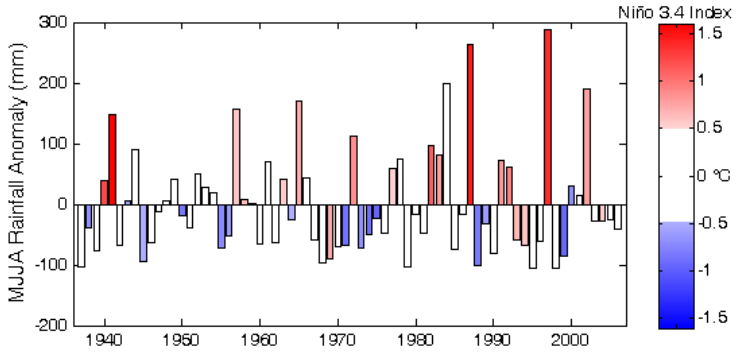

FIG. 8. Station-average MJJA rainfall amount, colored according to the sign and magnitude of the Niño 3.4 SST index for the period 1937–2005.

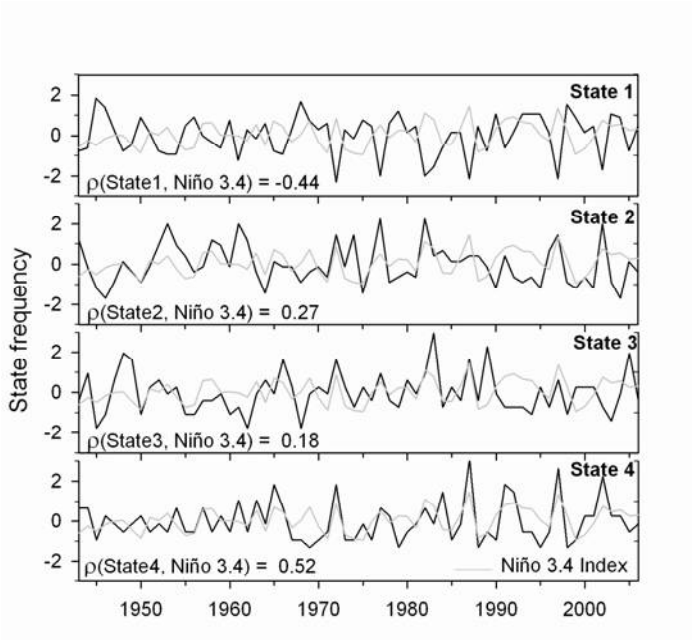

FIG. 9. Frequency of occurrence of each rainfall state over the 1943–2006 period (black line). The ENSO Niño 3.4 index is also plotted in each panel (grey line), together with the Pearson correlation coefficients (ρ). Standardized units.

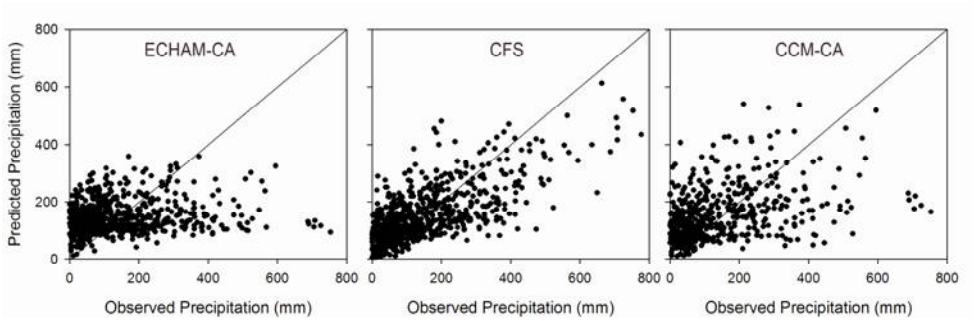

FIG. 10. Cross-validated hindcasts versus observed precipitation amounts using CCA for the three GCMs for the period 1981–2000, where each circle represents the value for each station, for each year. Thus there are 42x20 circles in each panel.

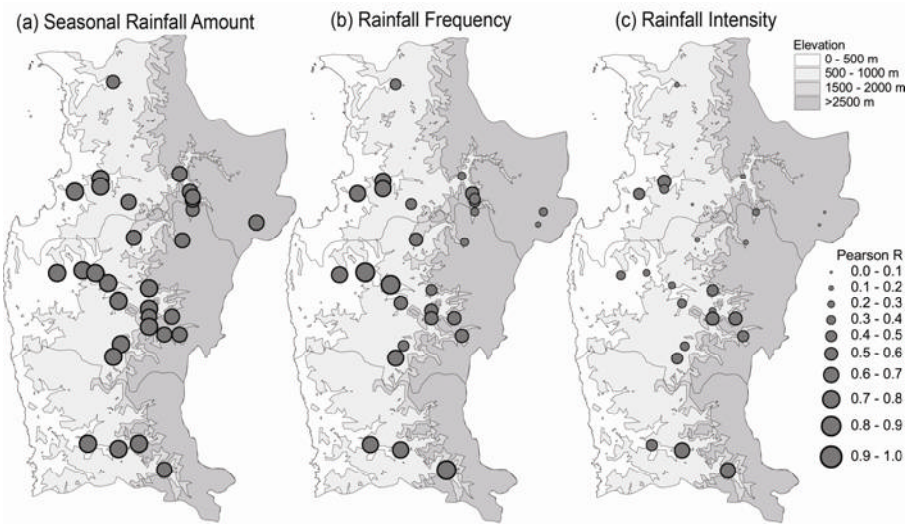

FIG. 11. Pearson correlation between CFS hindcasts downscaled using CCA and observed rainfall for (a) seasonal rainfall amount, (b) rainfall frequency, and (c) mean rainfall intensity, for the period 1981–2005.

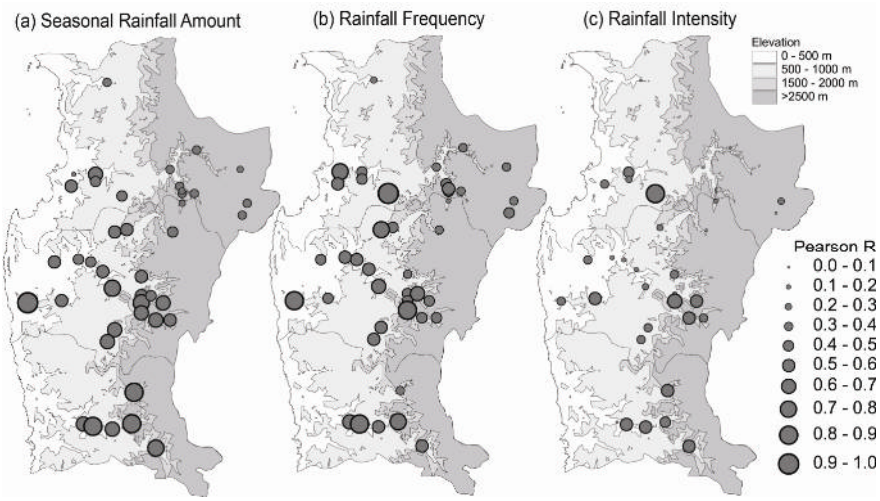

FIG. 12. As Fig. 11, but for CFS downscaled rainfall obtained using the nHMM and taking the ensemble mean over the 150 nHMM simulations.

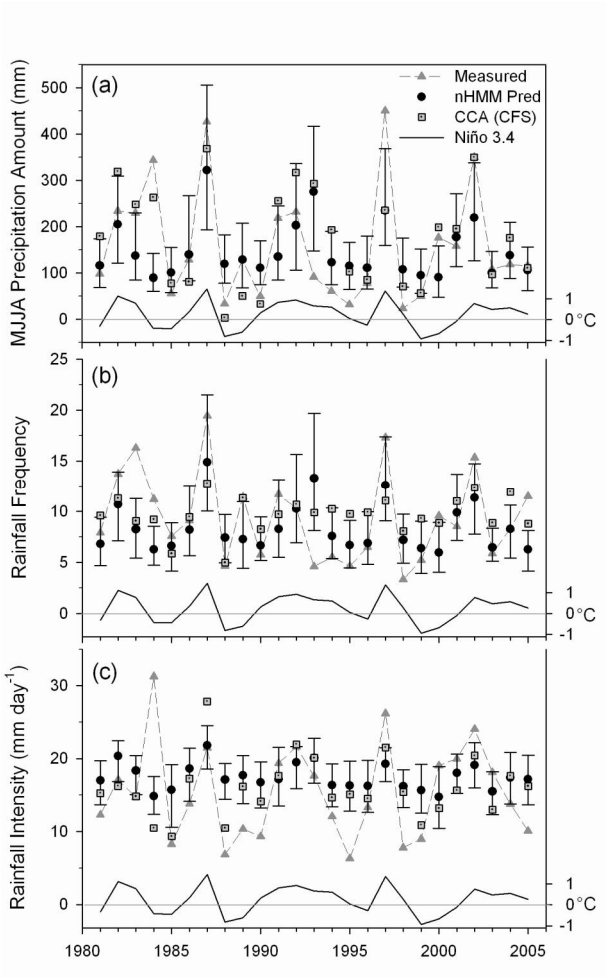

FIG. 13. Comparison of station-averaged downscaling results obtained from CFS using CCA and the nHMM. (a) seasonal rainfall amount, (b) rainfall frequency (b), mean rainfall intensity. The error bars indicate the 25th and 75th percentiles of the simulated nHMM ensemble values. The Niño 3.4 index is also indicated.

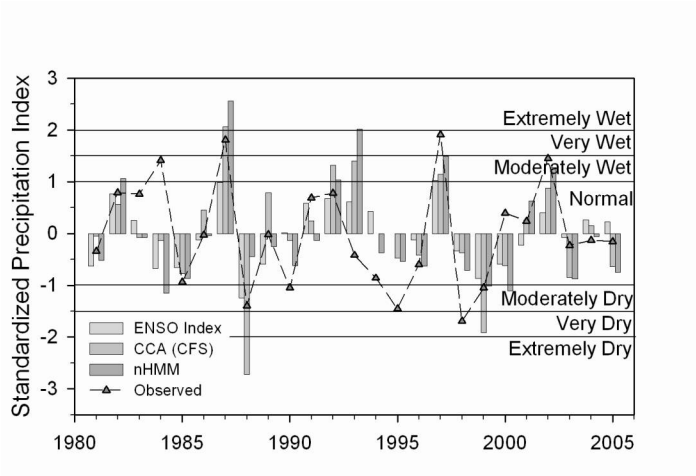

FIG. 14. Station-averaged hindcasts of the Standardized Precipitation Index (SPI) obtained from the MJJA Niño 3.4 Index, and the CFS downscaled with CCA and with the nHMM. The SPI values constructed from observed station rainfall are also plotted.

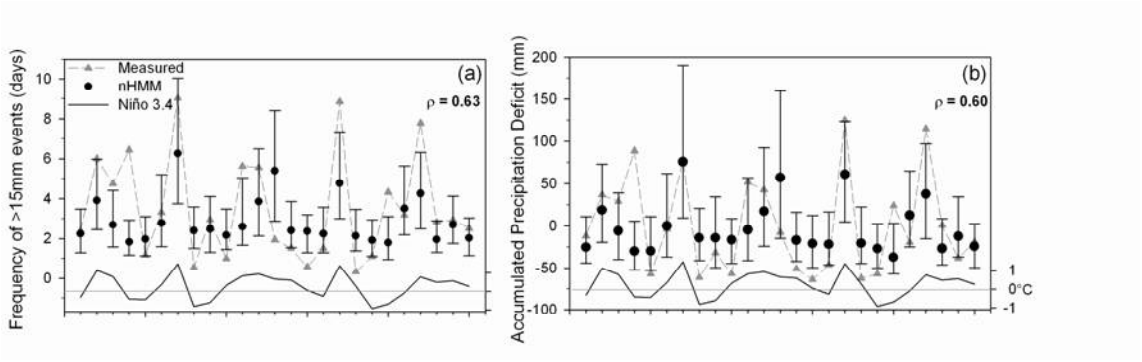

FIG. 15. Hindcasts of two station-averaged drought indices (circles) consisting of (a) the number of days with rainfall exceeding 15mm (FREQ15), and (b) and the Accumulated (daily) Precipitation Deficit (APD), based on the nHMM simulations, compared with values constructed from observed daily rainfall (dashed). The error bars indicate the 25th and 75th percentiles of the nHMM ensemble. The Niño 3.4 index is also indicated.

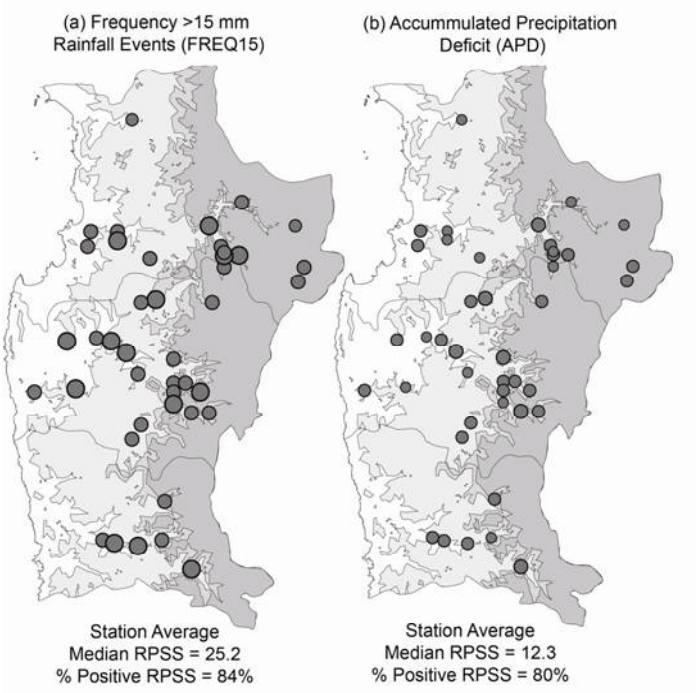

FIG. 16. Median Rank Probability Skill Score (RPSS) for hindcasts of a) the number of days with rainfall exceeding 15mm (FREQ15) and b) the Accumulated Precipitation Deficit (APD), constructed from the nHMM simulations.